

Ultrafast metal oxide reduction at Pd/PdO₂ interface enables onesecond hydrogen gas detection under ambient conditions

Xin Geng^{1,§}, Shuwei Li^{2,3,4,§}, Zhi Mei¹, Dongsheng Li⁵, Liang Zhang^{2,3,4} (), and Long Luo¹ ()

- ¹ Department of Chemistry, Wayne State University, Detroit, MI 48202, USA
- ² Center for Combustion Energy, Tsinghua University, Beijing 100084, China
- ³ School of Vehicle and Mobility, Tsinghua University, Beijing 100084, China
- ⁴ State Key Laboratory of Automotive Safety and Energy, Beijing 100084, China
- ⁵ Physical and Computational Sciences Directorate, Pacific Northwest National Laboratory, Richland, WA 99352, USA
- § Xin Geng and Shuwei Li contributed equally to this work.

© Battelle Memorial Institute under exclusive licence to Tsinghua University Press 2022

Received: 16 June 2022 / Revised: 21 July 2022 / Accepted: 22 July 2022

ABSTRACT

Here, we report a Pd/PdO_x sensing material that achieves 1-s detection of 4% H $_2$ gas (i.e., the lower explosive limit concentration for H $_2$) at room temperature in air. The Pd/PdO_x material is a network of interconnected nanoscopic domains of Pd, PdO, and PdO $_2$. Upon exposure to 4% H $_2$, PdO and PdO $_2$ in the Pd/PdO_x are immediately reduced to metallic Pd, generating over a > 90% drop in electrical resistance. The mechanistic study reveals that the Pd/PdO_x interface in Pd/PdO_x is responsible for the ultrafast PdO_x reduction. Metallic Pd at the Pd/PdO_x interface enables fast H $_2$ dissociation to adsorbed H atoms, significantly lowering the PdO_x reduction barrier. In addition, control experiments suggest that the interconnectivity of Pd, PdO, and PdO_x in our Pd/PdO_x sensing material further facilitates the reduction of PdO, which would otherwise not occur. The 1-s response time of Pd/PdO_x under ambient conditions makes it an excellent alarm for the timely detection of hydrogen gas leaks.

KEYWORDS

metal oxide reduction, Pd/PdO₂ interface, 1-s H₂ gas detection, ambient conditions

1 Introduction

Hydrogen (H₂) is an attractive fuel option for transportation and electricity generation applications because it is clean—water is the only product when used in a fuel cell—and can be produced from a variety of resources such as natural gas, biomass, or by water splitting using renewable power [1, 2]. Because H₂-air mixtures are highly explosive, the wide adoption of hydrogen fuel requires detecting the H₂ leakage immediately at the locations where H₂ is produced, stored, transported, and used [3]. Hence, the U.S. Department of Energy (DOE) has set target specifications for H₂ safety sensor research and development in terms of the measurement range (0.1% to 10%), operating temperature (-30 to 80 °C), response time (1 s), gas environment (ambient air, 10%-98% relative humidity), lifetime (10 years), and resistance to interferences (e.g., hydrocarbons) [4]. Among all the metrics, the response time (t_{response}) of 1-s in ambient air is the most challenging yet crucial [5]. Only a few H2 sensors have been reported to respond to 4% H₂ within 1-s (Table 1) [6-16]. These sensors can be generally summarized as the following two types: nanogap and plasmonic. As the name suggests, nanogap sensors contain nanoscopic gaps in the Pd sensing material. Upon exposure to H₂, Pd reacts with H₂ to form PdH₂. The expanded volume of PdH_x relative to Pd closes the nanogaps, resulting in a sudden electrical resistance drop. When the nanogaps are sufficiently small (< 50 nm), t_{response} can be as short as 75 ms [9]. For the plasmonic sensors, the sensor response arises from the shift of the localized surface plasmon resonance peak of Pd-based nanoarchitectures upon H_2 absorption by Pd. Their fast response was achieved by tailoring the volume-to-surface ratio in concert with reducing the apparent activation energy for H_2 absorption by engineering the metal–polymer coating interface [11, 12] and the sensing material composition [6, 11, 14, 15]. However, in these prior works, the 1-s response time was achieved either in an inert gas environment (e.g., N_2 and Ar) or under a vacuum, not in the ambient air required by the DOE. Pd-based sensors typically show degraded performance with reduced sensitivities and sluggish sensing speeds in the ambient air relative to the inert gas environment because O_2 competes with H_2 for surface sites, impeding H_2 reactions with Pd [3, 17].

Generally, there are two prerequisites to achieve ultrafast gas detection: first, rapid reaction kinetics between sensing material and gas analyte, and second, rapid transduction of the above reaction into a physical character that can be detected [18]. In this work, we chose to explore the hydrogen reduction of metal oxides to realize the 1-s detection of $4\%~H_2$ under ambient conditions because (1) metal oxide reduction is autocatalytic [19], meaning that once the reaction is initiated, it would self-accelerate and quickly complete; (2) $\rm O_2$ typically binds weakly to pure metal oxides, reducing its adverse impact on the $\rm H_2$ reactions with the sensing materials; and (3) the reduction of non-conducting or semiconducting metal oxides to conductive metals produces an instant and substantial electrical resistance drop, enabling effective

Table 1 Summary of the room-temperature hydrogen sensors with a response time $(t_{\text{response}}) \le 1$ s in the literature

Materials	Transducer platform	t_{response} (s)	Background environment	References
PdAu NP@PTEE/ PMMA	Optical	1	Vacuum	[11]
PdAuCu NP	Optical	0.4	Vacuum	[15]
TaPd thin film	Optical	0.5	Ar	[6]
POSS/Pd NP composite	Optical	1	Ar	[12]
PdCo alloy	Optical	0.85	N ₂ , vacuum	[14]
Pd mesowire	Electrical	0.075	N_2	[9]
Pd nanogap	Electrical	1	N_2	[10]
Pd nanogap	Electrical	1	N_2	[8]
Pd ultrathin film	Electrical	0.068	N_2	[13]
Pd NP on SiO_2 film	Capacitive	1	N_2	[7]
Pd/PdO_x (this work)	Electrical	1	Air	_

and rapid signal transduction. However, to initiate the direct reduction of metal oxides such as PdO, CuO, Cu₂O, Ag₂O, and NiO by H₂ is difficult at room temperature and often requires elevated temperatures to complete [19-24]. For example, the apparent activation energy for directly reducing Cu₂O by H₂ is about 27.4 kcal/mol, and the reduction process took ~ 180 min to complete, even at 230 °C. Introducing a metal (e.g., Pt, Pd, and Ru)/metal oxide interface is a possible solution to accelerating the initial metal oxide reduction kinetics [25, 26]. These metal/metal oxide interfaces have been reported to create highly reactive oxygen species due to the charge transfer between metal and oxide [27-38]. Moreover, the metal/metal oxide interface allows facile migration of atomic hydrogen readily dissociated by metals to metal oxides in close proximity (i.e., hydrogen spillover) [22, 39-41]. The reactive oxygen species and atomic hydrogen react quickly, resulting in the rapid reduction of metal oxide. Thus, tailoring the metal/metal oxide interface offers a unique opportunity to accomplish the challenging 1-s detection of H₂ under ambient conditions by rendering ultrafast metal oxide reduction kinetics.

Herein, we report a Pd/PdO_x material with ultrafast metal oxide reduction kinetics, enabling 1-s detection of 4% H₂ under ambient conditions. The Pd/PdO_x material was prepared by electrophoretically depositing Pd nanoparticles (NPs) onto a sensor substrate followed by in situ partial electrochemical oxidation of Pd to PdO, forming a network of interconnected nanoscopic domains of Pd, PdO, and PdO₂. Upon exposure to 4% H₂, PdO₂ is wholly reduced to metallic Pd, and PdO is partially reduced within just 1-s, leading to a > 90% drop in electrical resistance. The mechanistic study reveals that the Pd/PdO₂ interface is responsible for the fast reduction. More specifically, the presence of Pd shifts the rate-determining step for the PdO_x reduction from dissociative chemisorption of H2 molecules on PdO₂ to the diffusion of adsorbed H atom on PdO₂ by first dissociating H2 on metallic Pd, significantly lowering the activation energy barrier of PdO2 reduction from ~ 0.9 to ~ 0.6 eV.

Methods

2.1 Preparation of Pd NPs

Pd NPs were synthesized using a modified approach in the literature. Briefly, a 20 mL aqueous solution of 0.14 mmol potassium tetrachloropalladate(II) (Sigma Aldrich) was added to 400 mL of deionized (DI) water. After one minute, 10 mL aqueous solution of 0.84 mmol sodium citrate tribasic dehydrate (Sigma Aldrich) was added. After waiting for another minute, 5 mL of the freshly prepared ice-cold aqueous solution containing 0.14 mmol sodium borohydride (Sigma Aldrich) and 0.56 mmol sodium citrate tribasic dehydrate was added, and the reaction lasted for another 10 min. Before electrophoretic deposition, the assynthesized Pd NP solution was concentrated using a rotary evaporator by 2-fold to a final volume of ~ 200 mL and Pd NP concentration of $\sim 1.0 \,\mu\text{M}$.

2.2 Preparation of Pd/PdO_x sensors

The 1.0 µM Pd NP solution was used for electrophoretic deposition using a CHI 650E potentiostat, where a sensor substrate was used as the working electrode, a Pt foil (~ 385 mm²) as the counter electrode, and an Ag/AgCl electrode in saturated KCl as the reference electrode (Fig. S1 in the Electronic Supplementary Material (ESM)). The sensor substrate is an electrical insulator made of a sintered alumina plate with interdigitated Pt electrodes on one side. The distance between two neighboring Pt electrodes is 0.4 mm. Before electrophoretic deposition, the sensor substrates were washed with DI water and acetone and dried. Before use, the Pt foil was electrochemically polished in 0.5 M H₂SO₄ by running cyclic voltammograms between 1.1 and -0.23 V at a scan rate of 0.1 V/s for 50 cycles, followed by washing with DI water and acetone. Then, in a typical deposition, a positive potential was applied to the working electrode (merely immersing the interdigitated electrode part in the Pd NP solution) for 2 h. Subsequently, the deposited sensor substrate was removed from the reaction and dried in the air under ambient conditions. This work used four positive potentials of 1, 2, 5, and 10 V to prepare Pd/PdOx with different oxidation states. After H2 sensing test, the used Pd/PdOx sensors could also be partially regenerated by electrochemical oxidation at a high positive potential of 10 V in 0.1 M Na₂SO₄ aqueous solution for 20 min.

2.3 Preparation of other Pd sensing materials

Apart from potential regulation, the composition of the sensing materials was tuned by annealing Pd/PdO_x sensors at 400 °C in air for 1, 3, and 6 h using a hotplate (Thermo Scientific). For comparison, the Pd/PdO_x sensors were also heated in Ar at 400 °C for 6 h using a Schlenk flask.

1 mg powder of commercial PdO_x (PdO_x-c, Sigma Aldrich), Pd black (Pd black-c, Sigma Aldrich), or the mixture of PdO_x/Pd black in the molar ratio of 1:1 (PdO_x&Pd black-c mixture) were respectively dispersed in 100 µL ethanol to prepare their corresponding slurries. Next, 10 µL of the obtained slurries were drop-casted on the sensor substrate and then dried at ambient air naturally.

2.4 Gas sensing tests

The sensing measurements were carried out using a home-built apparatus at room temperature (22 °C). Specifically, the test setup consists of four parts: (1) gas cylinders of synthetic air and high purity of hydrogen (Airgas Co., Ltd); (2) mass flowrate controllers (MFC, Bronkhorst) for regulating gas flow rates; (3) data acquisition meter (Keysight/Agilent 34972A LXI) for measuring the electrical resistance in real-time; and (4) a PC connected to the meter for recording the resistance data. In a typical H₂ sensing test protocol, the Pd/PdO_x sensors were first stabilized in the air for 1 h at a constant flow rate of 1,000 sccm. When the sensors reached a constant electrical resistance of ca. 0.1 M Ω , the desired

concentration of H₂ in air flew over the sensors for 5 min. The total flow rate in this test was maintained at 1,000 sccm. The measurements for other interference gases in the selectivity study used the same protocol as H₂. The concentration for most of the interference gases was 4%, except H₂S (0.4 ppm), NO₂ (4 ppm), SO₂ (4 ppm), and ethylene (40 ppm). H₂S, NO, NO₂, SO₂, ethylene, and methane were purchased from Airgas Co., Ltd. The sources of the other interference gases were bought from Sigma Aldrich as high purity of liquids, and their concentrations were adjusted by the flow rate ratio of pure air and air bubbling through corresponding liquids. The relative humidity was calculated by the ratio of wet air (after bubbling through DI water) and dry air.

2.5 Material characterization

The surface morphology of the Pd/PdO_r sensors was collected using a JEOL JSM 7600F scanning electron microscopy (SEM). A JEOL 3100R05 transmission electron microscopy (TEM) (Double Cs Corrected TEM/STEM) was utilized to collect high-angle annular dark-field scanning transmission electron microscopy (HAADF-STEM) images for further structural characterization and analysis. The TEM samples were prepared by touching the deposited sensor surface using a TEM grid (carbon-coated 200-mesh Cu grids) to transfer the solid sample to the grid. Since the alumina and Pt electrode (the peak position close to Pd) from the sensor substrate has apparent interference with the analysis of Pd/PdO_x, Pd NPs were deposited on the carbon papers (FuelCellStore, SKU: 1594008-1) using the same protocol for the powder X-ray diffraction (PXRD) test (Bruker D2 Phaser diffractometer). X-ray diffraction patterns were analyzed using the powder diffraction file database of the International Center for Diffraction Data. X-ray photoelectron spectroscopy (XPS) characterizations were performed using an Al K-alpha X-ray photoelectron spectrometer (Thermo Scientific, K-alpha). XPS spectra were fitted by a composite function (30% Lorentzian + 70% Gaussian) using Avantage software. All the XPS spectra were calibrated using the C 1s peak at 284.8 eV.

2.6 Theoretical calculations

All calculations were performed via the Vienna *ab initio* simulation package utilizing density functional theory (DFT) [42, 43]. Core electrons were described using the projected-augmented wave (PAW) method [44]. The Kohn–Sham wave functions were expanded on a plane-wave basis with a kinetic energy cutoff of 400 eV to describe the valence electrons. The generalized gradient approximation using the Perdew–Burke–Ernzerhof functional was employed to evaluate the exchange-correlation energy [45].

The PdO (101) and PdO₂ (110) surfaces were modeled with a four-layer (2 × 4) PdO (101) supercell and PdO₂ (110) supercell, respectively. The bottom two layers of the surface were kept frozen, while the other layers and adsorbed gas molecules were set free to relax. A vacuum of > 14 Å was added to all surface models to ensure no appreciable interaction between periodic images. The Monkhorst-Pack scheme was employed to sample the Brillouin zone using a 3 \times 3 \times 1 k-point grid for atomic structure optimization [46]. The interface of PdO (or PdO₂) supported Pd nanoparticle is modeled by a periodic one-dimensional Pd rod deposited along the [010] direction of a PdO (101) slab (or PdO₂ (110) slab). For Pd/PdO and Pd/PdO2 models, a vacuum space of > 14 Å was added to prevent any appreciable interaction between periodic images. The Brillouin zone was sampled only on Gamma point for geometry optimization. All geometries were considered optimized when the force on each atom was < 0.025 eV/Å. The location and energy of transition states were calculated with the climbing-image nudged elastic band method [47, 48].

3 Results and discussion

3.1 Pd/PdO_x sensors preparation and characterization

Pd/PdO_x sensors were fabricated in one step by electrophoretically depositing citrate-capped Pd NPs onto a sensor substrate at a high potential of 10 V using a three-electrode setup (Fig. 1(a) and Fig. S1 in the ESM). Under the high potential of 10 V, the citrate ligands on Pd NPs were oxidatively removed once the NPs landed on the electrode, as evidenced by the disappearance of the C 1s peak at 288 eV in the XPS spectra of as-synthesized Pd/PdO_x (Fig. S2 in the ESM). The loss of ligand protection caused the NPs to aggregate into a porous network (NP size = 2.7 ± 0.3 nm and wire width = 6.6 ± 0.8 nm, Figs. 1(b)–1(d) and Fig. S3 in the ESM). The nanoporous chain-like morphology of electrophoretically deposited Pd/PdO_x resembles the nanoparticle aerogels, which are promising candidates in various applications due to their three-dimensional (3D) network structure, large surface area, and high porosity [49–51].

Analysis of high-resolution transmission electron microscopy (HRTEM) images reveals that the deposited Pd material is composed of interconnected nanoscopic domains of Pd, PdO, and PdO₂, as supported by the fast Fourier transform (FFT) diffraction patterns that match well with cubic Pd, tetragonal PdO, and tetragonal PdO₂ (Fig. 1(e)). The PXRD pattern also exhibits the signature peaks of Pd, PdO, and PdO₂, for example, the {111} peak for Pd, the {101} peak for PdO, and the {112} peak for PdO₂ in Fig. 1(f). As a reference, the Pd NP precursor only shows the PXRD peaks of Pd. Moreover, the XPS measurements demonstrated that a new Pd 3d_{5/2} peak emerged at ~ 337 eV (Fig. 1(g)), consistent with the PdO phase [52]. Numerical fitting of the XPS data reveals that Pd/PdO_x contains 29% Pd, 48% PdO, and 23% PdO₂ (Table S1 in the ESM). All the structural characterization data have confirmed the partial Pd oxidation to PdO and PdO₂ during the electrophoretic deposition process. The formation of PdO and PdO2 is expected because our electrode potential is higher than the equilibrium potential of a hydrated PdO and hydrated PdO₂ mixture (~ 1.23 V vs. standard hydrogen electrode) [53]. However, according to the Pourbaix diagram for Pd, Pd should not be thermodynamically stable at 10 V and $pH \approx 1$ (experimentally measured near the sensor substrate during electrodeposition) [54]. The co-existence of Pd, PdO, and PdO₂ phases in Pd/PdO_x is possible because the poor conductivity of PdO and PdO₂ (i.e., iR drop) lowers the potential applied on some Pd NPs, preventing the total conversion of Pd to PdO_r (Fig. 1(a)).

3.2 H₂ sensing performance

The performance of Pd/PdO_r sensors was tested using a homebuilt apparatus (Fig. S4 in the ESM). The response time $(t_{\rm response})$ was defined as the time required for the signal to vary by 90%. Strikingly, the Pd/PdO_x sensor resistance drops steeply by over 90% in 1 s upon exposure to 4% H_2 in ambient air (Fig. 2(a)). The same 1-s response time was observed in the sensing tests under an inert atmosphere (Fig. S5 in the ESM). The XRD and XPS analysis of the Pd/PdO_x sensor after H₂ exposure shows the complete reduction of PdO₂ to Pd and ~ 65% reduction of PdO to Pd (Fig. S6 and Table S2 in the ESM), confirming that the rapid PdO_x reduction is responsible for the ultrashort $t_{response}$ and high sensor response. The sensor does not recover after H2 removal because PdO_x reduction is irreversible. $t_{response}$ becomes longer and the sensor response decreases with decreasing H₂-concentration $(C_{\rm H_2})$ (Fig. 2(a) and Fig. S7 in the ESM). Relative humidity impacts the sensor performance: t_{response} is 1 s at a humidity level \leq 25% but gets longer at higher humidity levels (for example, ~ 4 s at 50%) due to the competitive adsorption between water vapor and H₂

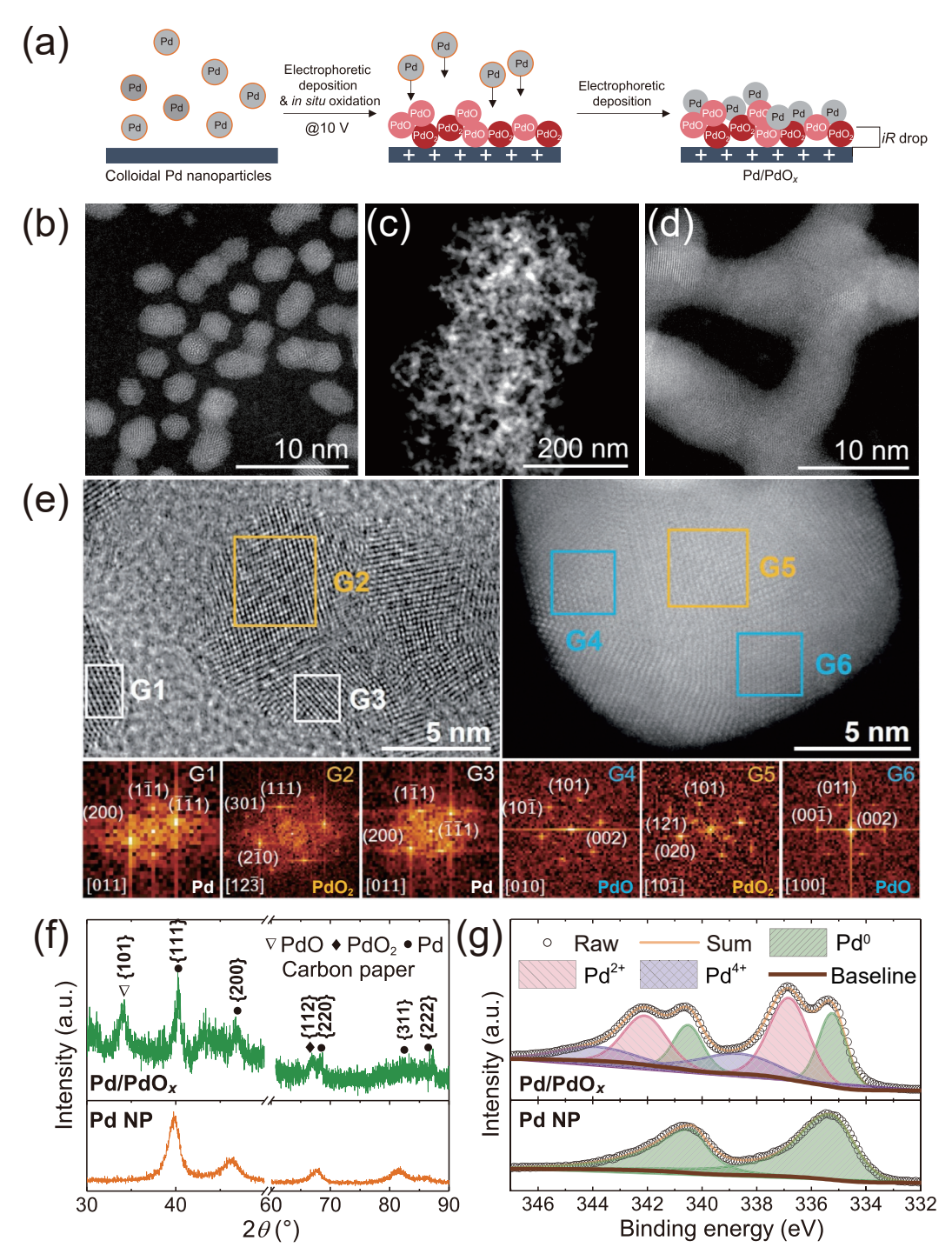


Figure 1 (a) Schematic illustration of the preparation of Pd/PdO_x sensors by electrophoretic deposition and partial in situ oxidation of Pd NPs. HAADF-STEM images of (b) Pd NPs, and (c) and (d) Pd/PdO_v electrophoretically deposited at 10 V (denoted as Pd/PdO_v). (e) Representative high-resolution TEM and STEM images of Pd/PdO_x, and the corresponding FFT diffraction patterns for the color-coded regions. White, yellow, and blue correspond to cubic Pd, tetragonal PdO, and tetragonal PdO₂, respectively. (f) PXRD patterns of Pd NPs and Pd/PdO_x. The peak assignments were based on the standard PDF cards of No. 00-046-1043 (cubic Pd), No. 00-041-1107 (tetragonal PdO), and No. 00-034-1101 (tetragonal PdO₂). (g) XPS spectra showing the Pd 3d region of Pd NPs and Pd/PdO₂.

onto the sensor surface. However, relative humidity did not change the sensor response (Fig. 2(b) and Fig. S8 in the ESM).

Next, we assessed the cross-sensitivity of the Pd/PdO_x sensor toward 32 different interference gases, including CO, NO₂, NO, SO₂, H₂S, NH₃, and various organic gas and vapors such as natural gas, hexane, benzene, formaldehyde, and methanol. All interference gases have a concentration of 4% in air, except for H₂S (0.4 ppm), NO₂, NO, and SO₂ (4 ppm for each), and ethylene (40 ppm). The interference test results show that the Pd/PdO_x sensors only exhibit weak cross-sensitivity (~ 10% to 30%) toward CO, CH₄, and NH₃, and negligible response (< 5%) to other interference gases relative to H₂ (Fig. 2(c) and Fig. S9 in the ESM).

The weak cross-sensitivity to CO and CH₄ is because CO and CH₄ can partially reduce PdO_x to Pd, but much less than H₂. Interestingly, Pd/PdO_x also reacts with CO and CH₄ differently: CO reacted mostly with PdO, whereas CH₄ selectively reacted with PdO₂ (Fig. S10 and Table S3 in the ESM). These findings are consistent with the literature reports that different Pd-O species exhibit different reactivities toward CO and CH₄ [52, 55, 56]. Pd, PdO, or a Pd/PdO mixed phase is not active for CH₄ activation at room temperature [52]. In comparison, adsorbed O on metallic Pd could be reduced by CO within a few minutes at a temperature as low as 223 K, while the more deeply oxidized Pd was much less reactive and required an elevated temperature [56]. Because of

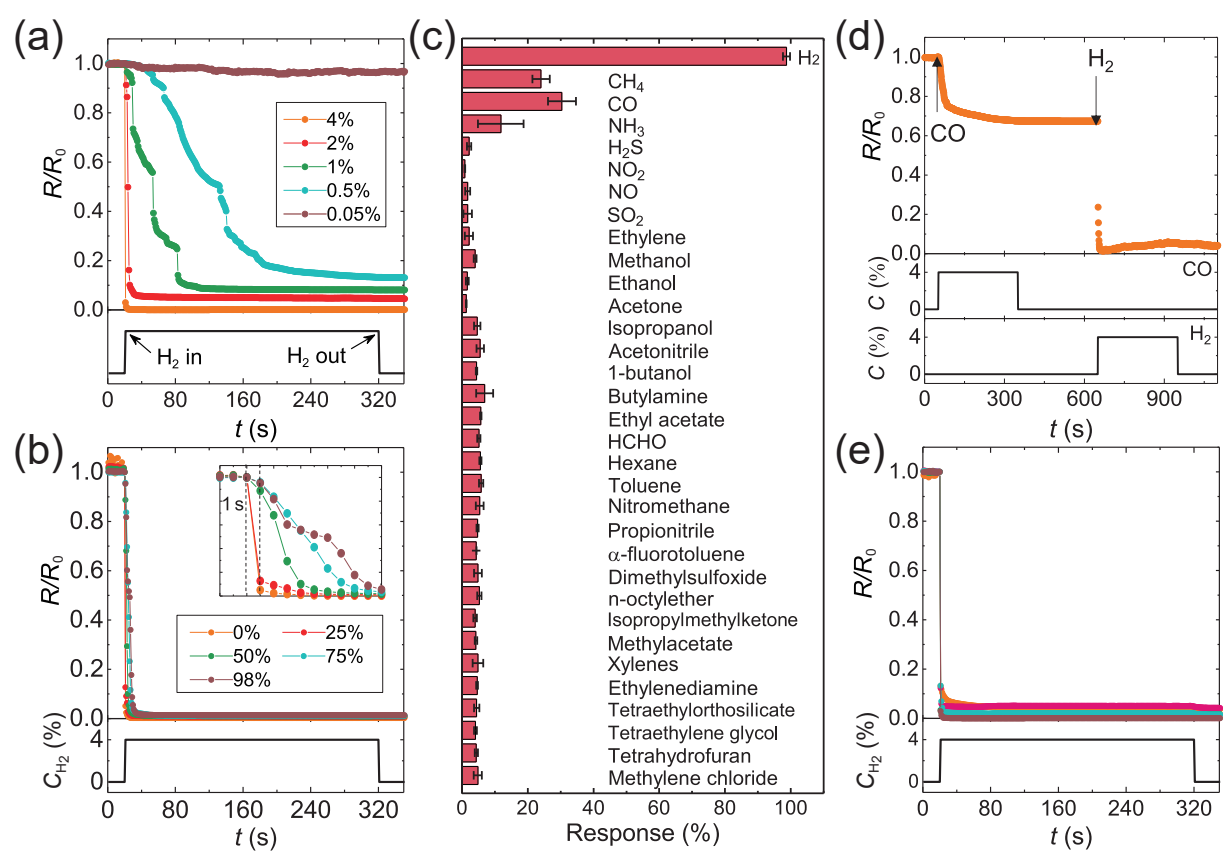


Figure 2 (a) Dynamic sensing resistance curves of Pd/PdO_x in response to H_2 at different concentrations (0.05%–4%) at room temperature in air. The data acquisition rate is 1 Hz, meaning each data point is 1 s. R_0 is the baseline resistance. (b) Humidity dependence of Pd/PdO_x towards 4% H_2 with humidity ranging from 0% to 98% at room temperature. The inset shows the response–recovery curve in the first ten seconds upon exposure to H_2 gas. (c) The percentage change of sensor response upon exposure to 32 different interference gases. The concentrations of interference gases are 4%, except for ethylene (40 ppm), NO_2 (4 ppm), NO_2 (4 ppm), NO_2 (4 ppm), and NO_2 (4 ppm), and NO_2 (4 ppm), and NO_2 (10 ppm) are NO_2 (10 ppm), and NO_2 (11 ppm) are NO_2 (12 ppm), and NO_2 (13 ppm) are NO_2 (14 ppm), and NO_2 (15 ppm) are NO_2 (16 ppm), and NO_2 (17 ppm) are NO_2 (17 ppm) are NO_2 (17 ppm), and NO_2 (18 ppm) are NO_2 (19 ppm), and NO_2 (19 ppm) are NO_2 (19 ppm), and NO_2 (19 ppm) are NO_2 (19 p

such reactivity differences, the Pd/PdOx sensor could still show a rapid (~ 3 s) and significant response (> 70%) to 4% H₂ even after being exposed to 4% CO for 5 min (Fig. 2(d)), indicating the excellent CO-poisoning tolerance of the Pd/PdO_x sensor. For NH₃, the composition of Pd/PdO_x did not show a noticeable change after the test (Fig. S10 and Table S3 in the ESM), suggesting that the sensor response did not arise from PdO_x reduction. The sensor resistance increased after introducing NH₃ and partially recovered once NH3 was removed (Fig. S9 in the ESM), which is characteristic of a p-type semiconductor gas sensor in response to a reducing gas analyte such as NH₃ [57], consistent with the p-type semiconductor characteristics of PdO [58, 59]. It is also worth noting that the reaction kinetics between CO, CH₄, and NH₃ with Pd/PdO_x are much slower than H₂, taking at least ten times longer to complete (Fig. S9 in the ESM). Moreover, our onestep electrophoretic synthesis simplifies the sensor fabrication, undoubtedly lowering the production cost and ensuring reproducibility among devices. Indeed, we tested five independently prepared Pd/PdO_r sensors and found a remarkably low device-to-device sensor response variation of < 3% and a constant t_{response} of 1-s (Fig. 2(e)).

3.3 Mechanistic understanding

The exceptionally rapid response of Pd/PdO_x sensors to H_2 undoubtedly results from the ultrafast PdO_x reduction kinetics. However, Pd/PdO_x 's complex structure makes it challenging to pinpoint the active sites responsible for the fast reduction. Thus, we started the mechanistic study by investigating the composition effect on $t_{response}$. The composition of Pd/PdO_x was varied by applying different electrode potentials during electrophoretic

deposition. The XPS results show that the Pd/PdO_x materials prepared under 1, 2, 5, and 10 V were all composed of Pd, PdO, and PdO2 and citrate ligands were also removed during electrosynthesis for all samples (Figs. S2 and S11 in the ESM). As the electrode potential increased from 1 to 10 V, the Pdo content gradually decreased from 43% to 29%, PdO2 increased from 12% to 23%, and PdO stayed at ~ 50% (Table S1 in the ESM). Upon exposure to 4% H₂ in air, all Pd/PdO_x sensors exhibited a substantial resistance decrease due to the PdO_x reduction to metallic Pd (Fig. 3(a), Figs. S12 and S13, and Table S2 in the ESM). However, two noticeable differences exist between the response curves of the Pd/PdO_x sensors prepared at 5 and 10 V and those prepared at 1 and 2 V (Fig. 3(a)). First, t_{response} of the 1 and 2 V sensors (6 and 11 s, respectively) are much longer than the 1 s of the 5 and 10 V ones. Second, their responses are also smaller. Because the compositional differences among these samples were mainly from Pd and PdO₂, it is reasonable to speculate that Pd and PdO2 are the two critical ingredients in Pd/PdO2 to achieve fast reduction.

To test our speculation, we first thermally annealed the Pd/PdO_x in the air to eliminate metallic Pd by oxidizing it to PdO and PdO_2 . After thermal treatment for 6 h, Pd in Pd/PdO_x was converted to PdO and PdO_2 (PdO: 67.1% and PdO_2 : 32.9%, Fig. S14 and Table S4 in the ESM). The sensing response of thermally treated Pd/PdO_x was utterly different from that of the initial Pd/PdO_x . For the 6-h sample, the sensor showed the typical behavior of a p-type semiconductor gas sensor: The electrical resistance increased in response to H_2 with $t_{response}$ of 32 s at 4% H_2 (Fig. 3(b)). PdO_x was also not reduced to metallic Pd after exposure to 4% H_2 for 5 min (Fig. S15 and Table S4 in the ESM).

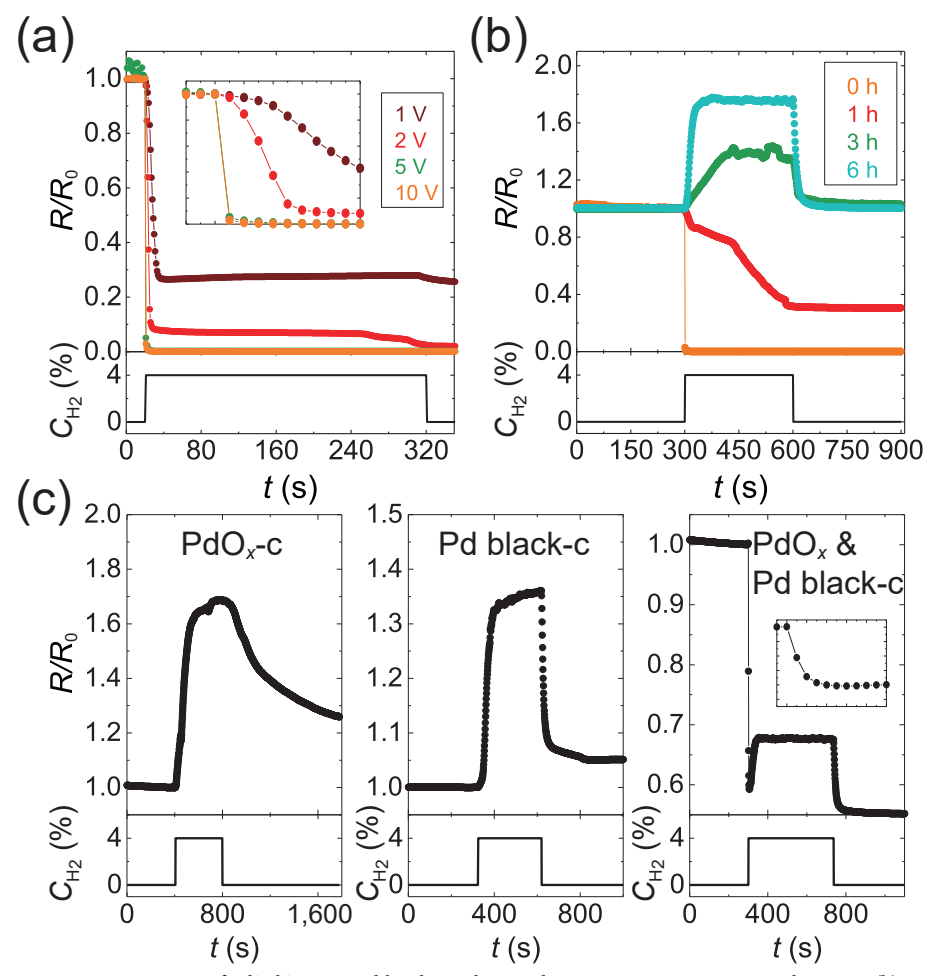


Figure 3 (a) Dynamic sensing resistance curves of Pd/PdO_x prepared by electrophoretic deposition using 1–10 V towards 4% H_2 . (b) Dynamic sensing resistance curves at 4% H_2 for the Pd/PdO_x samples after thermal treatment at 400 °C for 1, 3, and 6 h in air. (c) Dynamic sensing resistance curves of PdO_x -c, Pd black, and the physical mixture of the two PdO_x -dependent of the two PdO_x -dependent of the first ten seconds upon exposure to PdO_x -c. (b) Dynamic sensing resistance curves of PdO_x -c. (c) Dynamic sensing resistance curves of PdO_x -c. (d) Dynamic sensing resistance curves of PdO_x -c. (e) Dynamic sensing resistance curves of PdO_x -c. (f) Dynamic sen

For Pd/PdO_x samples with 1- and 3-h-long thermal treatment, their sensing behaviors lay between semiconductor sensing and metal oxide reduction sensing (Fig. 3(b)). The same p-type semiconductor sensing characteristics and no oxide reduction were observed for PdO_x-c with a similar chemical composition of PdO: 72.7% and PdO₂: 27.3% (Fig. 3(c), and Fig. S17, and Tables S5 and S6 in the ESM). The above observations are consistent with the literature report that the onset of the reduction of pure metal oxides such as PdO occurs at temperatures higher than 500-700 K [60]. We also carried out a control experiment by annealing Pd/PdO_x in Ar at 400 °C for 6 h. The annealed sample largely retained its composition and showed similar metal oxide reduction sensing behavior as the untreated sensors (Fig. S16 and Table S4 in the ESM). The above results show that the presence of metallic Pd is critical to initiating the rapid reduction of PdO_x at room temperature.

Next, we attempted to prepare Pd/PdO with similar morphology as Pd/PdO_x at potentials lower than 1 V to prove the essential role of PdO_2 in the rapid PdO_x reduction. However, the incomplete removal of citrate ligands from the Pd surface during the electrophoretic deposition at 1 V led to inconclusive results. Therefore, we turned to the commercial ligand-free Pd black containing 46.5% Pd and 53.5% PdO (Pd black-c, Fig. S17 and Table S5 in the ESM). The Pd black-c sensor exhibited p-type semiconductor sensing behavior (Fig. 3(c)), the same as other Pd/PdO sensors reported in Refs. [61, 62]. Furthermore, the XPS analysis revealed that the PdO content of Pd black did not change after exposure to 4% H_2 (Fig. S17 and Table S6 in the ESM),

indicating that H₂ reduction of PdO is insignificant even in the presence of Pd⁰ at room temperature.

Thus far, our compositional study has shown that neither Pd/PdO nor PdO/PdO₂ could effectively react with 4% H₂ at room temperature to form metallic Pd, supporting that Pd and PdO2 are responsible for the rapid reduction. However, we did not consider the possible contributions of the unique nanostructures of Pd/PdO_x to the rapid oxide reduction at room temperature, which could be significant. Thus, to assess whether the unique nanostructure of Pd/PdO_x (i.e., interconnected nanodomains of Pd, PdO, and PdO2) indeed plays a critical role in the rapid reduction of PdO, we prepared a composite of Pd, PdO, and PdO₂ by physically mixing commercial Pd black and PdO_x-c. The PdO_x&Pd black-c composite has a similar composition $(Pd:PdO:PdO_2 = 23\%:63\%:14\%)$ as our Pd/PdO_x material but without the nanoscopic structural features. Intriguingly, the PdO,&Pd black-c sensor showed a similar rapid resistance drop by 40% in the first 3 s as the Pd/PdO_x sensor (Fig. 3(c)). XPS result shows that the resistance drop was exclusively caused by the reduction of PdO2 to metallic Pd, and the PdO content did not change (Fig. S17 and Table S6 in the ESM). After the initial 3 s, the unreduced PdO in PdO,&Pd black-c gave the p-type semiconductor sensing response (Fig. 3(c)). These results indicate that (1) when Pd and PdO2 are adjacent either via grain boundaries as in Pd/PdO_x samples (Fig. 1(e)) or simply physical contact as in the PdO_x&Pd black-c, they can trigger the rapid reduction of PdO2; and (2) the interconnected nanodomains of

Pd, PdO, and PdO $_2$ enable the reduction of PdO by 4% H_2 at room temperature which would otherwise not occur.

To unravel the mechanism behind the rapid PdO_x reduction caused by the Pd/PdO₂ interface, we carried out DFT calculations of the energy profiles for metal oxide reaction with H₂ on a PdO₂ (110) surface, a PdO (101) surface, a Pd (111)/PdO₂ (110) interface, and a Pd (111)/PdO (101) interface (Fig. 4). The calculated energy profiles in Figs. 4(a) and 4(b) show that the PdO₂ (110) and PdO (101) surfaces have different ratedetermining steps (RDS): H₂* dissociation for PdO₂ (110) and H* diffusion for PdO (101). For the Pd (111)/PdO₂ (110) interface, the sluggish H₂* dissociation on PdO₂ (110) is bypassed by the alternative low-barrier pathway on Pd (111) surface (H2* dissociation energy: $0.92 \text{ eV} \rightarrow 0.12 \text{ eV}$, Fig. 4(c)). The energy barriers for H* diffusing from Pd (111) to PdO₂ (110) surface and subsequent H₂O* formation process were 0.60 and 0.22 eV, respectively (S3 \rightarrow S4 and S4 \rightarrow S5 in Fig. 4(c)). Therefore, the RDS for PdO₂ reduction switches from H₂* dissociation to H* diffusion when Pd/PdO₂ interface is present. We have also found another possible H* diffusion pathway from Pd to PdO2 via a bridging binding geometry of H* at the Pd/PdO2 interface, which could further reduce the diffusion energy barrier to 0.40 eV (Fig. S18 in the ESM). In contrast, although accelerated H₂* dissociation on Pd also took place at the Pd (111)/PdO (101) interface, the H* diffusion remains as the RDS for PdO reduction (Fig. 4(d)), suggesting that the reduction kinetics of PdO (101) benefit much less from the Pd/PdO interface. The above DFT results clearly explain the essential role of Pd/PdO₂ interface in achieving ultrafast metal oxide reduction, in excellent agreement with experimental observation in Fig. 3.

4 Conclusions

In conclusion, we reported a Pd/PdO_x material with ultrafast hydrogen reduction kinetics, enabling 1-s detection of 4% H₂ in ambient air. The mechanistic study reveals that the Pd/PdO₂ interface in Pd/PdOx is responsible for the rapid reduction of PdO₂. The presence of metallic Pd allows rapid H₂ dissociation to adsorbed H atoms, overcoming the RDS in PdO2 reduction. In contrast, because the RDS of PdO reduction is the adsorbed H atom diffusion on PdO, not the H2 dissociation, PdO reduction does not benefit from the facile H2 dissociation at the Pd/PdO interface. However, the interconnectivity of Pd, PdO, and PdO2 in Pd/PdO_x enables the reduction of PdO, which would otherwise not occur. Due to the irreversible nature of PdO_x reduction to Pd, the Pd/PdO_x sensor does not recover after H₂ exposure and thus can only be used as an H2 alarm. Although the Pd/PdOx sensors can be partially regenerated and recycled after use by electrochemical oxidation at 10 V for 20 min (Figs. S19 and S20, and Table S7 in the ESM), the typical response time becomes 2-5 s. We are now exploring other combinations of metal and high-valance metal oxide to develop 1-s response time H2 alarms that can be completely "reset" by regenerating the metal oxide after the alarm is triggered.

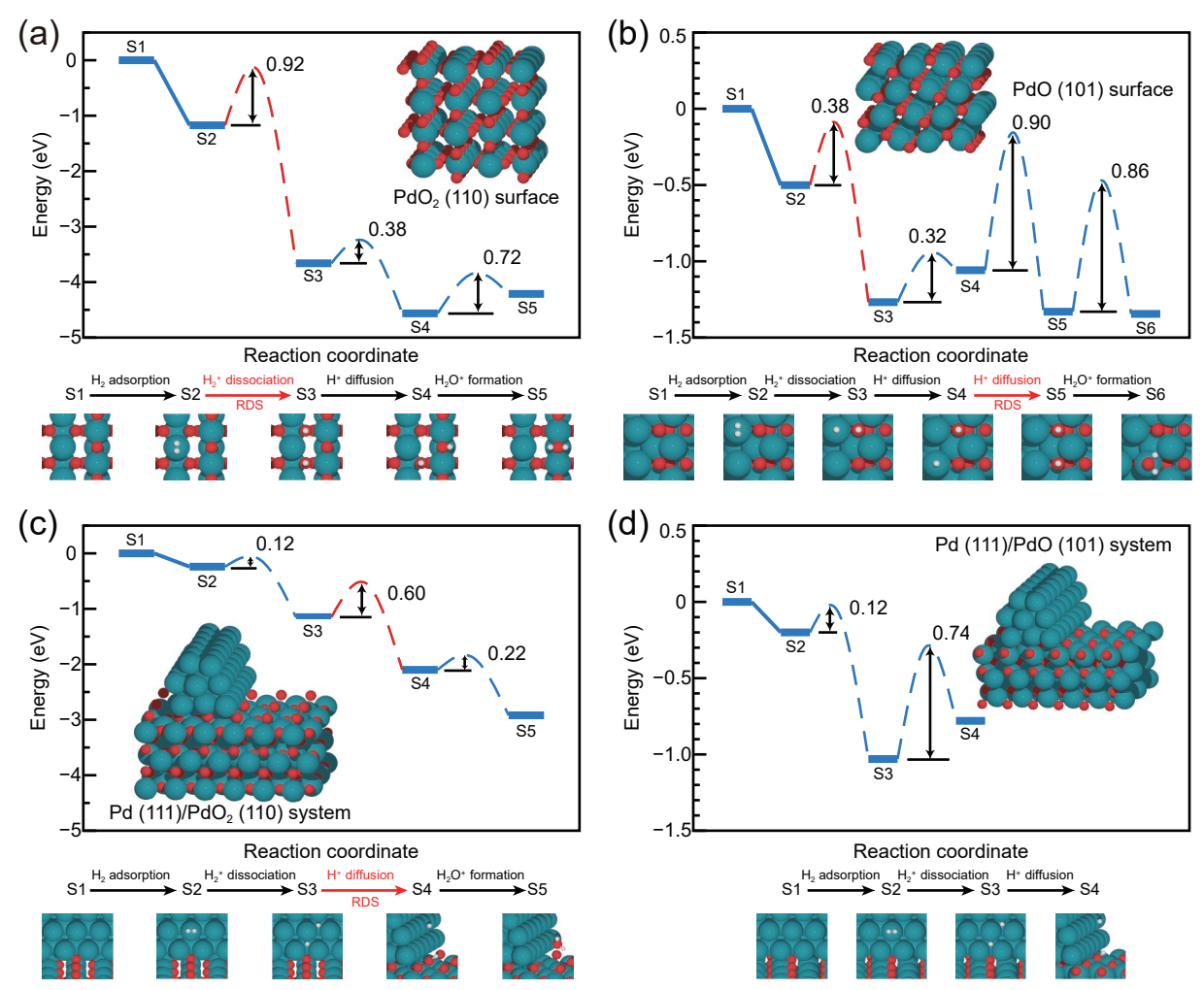


Figure 4 DFT-calculated energy profiles for hydrogen reduction of PdO and PdO₂ to form water on (a) PdO₂ (110) surface, (b) PdO (101) surface, (c) Pd NP on a PdO₂ surface containing a Pd (111)/PdO₂ (110) interface, and (d) Pd NP on a PdO surface containing a Pd (111)/PdO (101) interface. The configurations at the bottom show a schematic representation of reactants and products in every reaction step. Cyan, red, and white balls represent Pd, O, and H atoms, respectively.

Acknowledgements

The work at Wayne State University and the Pacific Northwest National Laboratory was supported by the U.S. Department of Energy (DOE), Office of Science, Office of Basic Energy Sciences, through Award # 78705. In addition, L. L. and X. G. acknowledge support from National Science Foundation under award CHE-1943737. L. Z. and S. W. L. acknowledge support from the National Natural Science Foundation of China (No. 22103047) and Hefei National Laboratory for Physical Sciences at the Microscale (No. KF2020107). We also thank Prof. Reg Penner at the University of California, Irvine, for his valuable suggestions.

Electronic Supplementary Material: Supplementary material (further details of the SEM, XPS, XRD measurements, gas sensing test apparatus, gas sensing performance, DFT calculation results, and XPS analysis) is available in the online version of this article at https://doi.org/10.1007/s12274-022-4816-2.

References

- [1] Hydrogen to the rescue. Nat. Mater. 2018, 17, 565.
- [2] Zhu, P.; Xiong, X.; Wang, D. S. Regulations of active moiety in single atom catalysts for electrochemical hydrogen evolution reaction. Nano Res. 2022, 15, 5792-5815.
- Koo, W. T.; Cho, H. J.; Kim, D. H.; Kim, Y. H.; Shin, H.; Penner, R. M.; Kim, I. D. Chemiresistive hydrogen sensors: Fundamentals, recent advances, and challenges. ACS Nano 2020, 14, 14284-14322.
- [4] U. S. Department of Energy, Energy Efficiency and Renewable Energy (EERE), Fuel Cell Technologies Office. Multi-Year Research, Development, and Demonstration Plan, 2011-2020. Section 3.7 Hydrogen Safety, Codes and Standards (EERE, 2015).
- [5] Hübert, T.; Boon-Brett, L.; Black, G.; Banach, U. Hydrogen sensors—A review. Sens. Actuators B 2011, 157, 329-352.
- [6] Bannenberg, L.; Schreuders, H.; Dam, B. Tantalum-palladium: Hysteresis-free optical hydrogen sensor over 7 orders of magnitude in pressure with sub-second response. Adv. Funct. Mater. 2021, 31. 2010483.
- [7] Pour, G. B.; Aval, L. F.; Esmaili, P. Performance of gas nanosensor in 1-4 per cent hydrogen concentration. Sens. Rev. 2019, 39, 622 - 628
- [8] Chang, T.; Jung, H.; Jang, B.; Lee, J.; Noh, J. S.; Lee, W. Nanogaps controlled by liquid nitrogen freezing and the effects on hydrogen gas sensor performance. Sens. Actuators A: Phys. 2013, 192, 140-144.
- [9] Favier, F.; Walter, E. C.; Zach, M. P.; Benter, T.; Penner, R. M. Hydrogen sensors and switches from electrodeposited palladium mesowire arrays. Science 2001, 293, 2227-2231.
- [10] Lee, J.; Noh, J. S.; Lee, S. H.; Song, B.; Jung, H.; Kim, W.; Lee, W. Cracked palladium films on an elastomeric substrate for use as hydrogen sensors. Int. J. Hydrogen Energy 2012, 37, 7934-7939
- [11] Nugroho, F. A. A.; Darmadi, I.; Cusinato, L.; Susarrey-Arce, A.; Schreuders, H.; Bannenberg, L. J.; da Silva Fanta, A. B.; Kadkhodazadeh, S.; Wagner, J. B.; Antosiewicz, T. J. et al. Metalpolymer hybrid nanomaterials for plasmonic ultrafast hydrogen detection. Nat. Mater. 2019, 18, 489-495.
- [12] Sirbuly, D. J.; Létant, S. E.; Ratto, T. V. Hydrogen sensing with subwavelength optical waveguides via porous silsesquioxanepalladium nanocomposites. Adv. Mater. 2008, 20, 4724-4727.
- [13] Xu, T.; Zach, M. P.; Xiao, Z. L.; Rosenmann, D.; Welp, U.; Kwok, W. K.; Crabtree, G. W. Self-assembled monolayer-enhanced hydrogen sensing with ultrathin palladium films. Appl. Phys. Lett. 2005, 86, 203104.
- [14] Luong, H. M.; Pham, M. T.; Guin, T.; Madhogaria, R. P.; Phan, M. H.; Larsen, G. K.; Nguyen, T. D. Sub-second and ppm-level optical sensing of hydrogen using templated control of nano-hydride geometry and composition. Nat. Commun. 2021, 12, 2414.
- [15] Darmadi, I.; Nugroho, F. A. A.; Kadkhodazadeh, S.; Wagner, J. B.; Langhammer, C. Rationally designed PdAuCu ternary alloy

- nanoparticles for intrinsically deactivation-resistant ultrafast plasmonic hydrogen sensing. ACS Sens. 2019, 4, 1424-1432.
- [16] Lee, J.; Shim, W.; Lee, E.; Noh, J. S.; Lee, W. Highly mobile palladium thin films on an elastomeric substrate: Nanogap-based hydrogen gas sensors. Angew. Chem., Int. Ed. 2011, 50, 5301-5305.
- [17] Koo, W. T.; Qiao, S. P.; Ogata, A. F.; Jha, G.; Jang, J. S.; Chen, V. T.; Kim, I. D.; Penner, R. M. Accelerating palladium nanowire H₂ sensors using engineered nanofiltration. ACS Nano 2017, 11, 9276-9285
- [18] Yamazoe, N. Toward innovations of gas sensor technology. Sens. Actuators B: Chem. 2005, 108, 2-14.
- [19] Rukini, A.; Rhamdhani, M. A.; Brooks, G. A.; Van den Bulck, A. Metals production and metal oxides reduction using hydrogen: A review. J. Sustainable Metall. 2022, 8, 1-24.
- [20] Kim, J. Y.; Rodriguez, J. A.; Hanson, J. C.; Frenkel, A. I.; Lee, P. L. Reduction of CuO and Cu2O with H2: H embedding and kinetic effects in the formation of suboxides. J. Am. Chem. Soc. 2003, 125, 10684-10692
- [21] Su, S. C.; Carstens, J. N.; Bell, A. T. A study of the dynamics of Pd oxidation and PdO reduction by H₂ and CH₄. J. Catal. 1998, 176, 125-135.
- [22] O'Connor, C. R.; van Spronsen, M. A.; Egle, T.; Xu, F.; Kersell, H. R.; Oliver-Meseguer, J.; Karatok, M.; Salmeron, M.; Madix, R. J.; Friend, C. M. Hydrogen migration at restructuring palladium-silver oxide boundaries dramatically enhances reduction rate of silver oxide. Nat. Commun. 2020, 11, 1844.
- [23] Manukyan, K. V.; Avetisyan, A. G.; Shuck, C. E.; Chatilyan, H. A.; Rouvimov, S.; Kharatyan, S. L.; Mukasyan, A. S. Nickel oxide reduction by hydrogen: Kinetics and structural transformations. J. Phys. Chem. C 2015, 119, 16131-16138.
- [24] Martin, N. M.; Van den Bossche, M.; Grönbeck, H.; Hakanoglu, C.; Gustafson, J.; Blomberg, S.; Arman, M. A.; Antony, A.; Rai, R.; Asthagiri, A. et al. Dissociative adsorption of hydrogen on PdO (101) studied by HRCLS and DFT. J. Phys. Chem. C 2013, 117, 13510-13519
- [25] Li, R. Z.; Wang, D. S. Understanding the structure-performance relationship of active sites at atomic scale. Nano Res. 2022, 15, 6888-6923
- [26] Zhang, Z. D.; Zhou, M.; Chen, Y. J.; Liu, S. J.; Wang, H. F.; Zhang, J.; Ji, S. F.; Wang, D. S.; Li, Y. D. Pd single-atom monolithic catalyst: Functional 3D structure and unique chemical selectivity in hydrogenation reaction. Sci. China Mater. 2021, 64, 1919-1929.
- [27] Bliem, R.; van der Hoeven, J.; Zavodny, A.; Gamba, O.; Pavelec, J.; de Jongh, P. E.; Schmid, M.; Diebold, U.; Parkinson, G. S. An atomic-scale view of CO and H2 oxidation on a Pt/Fe3O4 model catalyst. Angew. Chem., Int. Ed. 2015, 54, 13999-14002.
- [28] Brown, M. K.; Degrado, S. J.; Hoveyda, A. H. Highly enantioselective Cu-catalyzed conjugate additions of dialkylzinc reagents to unsaturated furanones and pyranones: Preparation of airstable and catalytically active Cu-peptide complexes. Angew. Chem., Int. Ed. 2005, 44, 5306-5310.
- [29] Carrettin, S.; Concepción, P.; Corma, A.; Nieto, J. M. L.; Puntes, V. F. Nanocrystalline CeO₂ increases the activity of Au for CO oxidation by two orders of magnitude. Angew. Chem., Int. Ed. 2004, 43, 2538-2540.
- [30] Falsig, H.; Hvolbæk, B.; Kristensen, I. S.; Jiang, T.; Bligaard, T.; Christensen, C. H.; Nørskov, J. K. Trends in the catalytic CO oxidation activity of nanoparticles. Angew. Chem., Int. Ed. 2008, 47, 4835-4839
- [31] Remediakis, I. N.; Lopez, N.; Nørskov, J. K. CO oxidation on rutilesupported Au nanoparticles. Angew. Chem., Int. Ed. 2005, 44,
- [32] Rodriguez, J. A.; Graciani, J.; Evans, J.; Park, J. B.; Yang, F.; Stacchiola, D.; Senanayake, S. D.; Ma, S. G.; Pérez, M.; Liu, P. et al. Water-gas shift reaction on a highly active inverse CeO_x/Cu (111) catalyst: Unique role of ceria nanoparticles. Angew. Chem., Int. Ed. **2009**. 48, 8047–8050.
- [33] Puigdollers, A. R.; Schlexer, P.; Tosoni, S.; Pacchioni, G. Increasing oxide reducibility: The role of metal/oxide interfaces in the formation of oxygen vacancies. ACS Catal. 2017, 7, 6493-6513.

[34] Shao, X.; Prada, S.; Giordano, L.; Pacchioni, G.; Nilius, N.; Freund, H. J. Tailoring the shape of metal Ad-particles by doping the oxide support. *Angew. Chem., Int. Ed.* 2011, 50, 11525–11527.

- [35] Sterrer, M.; Yulikov, M.; Fischbach, E.; Heyde, M.; Rust, H. P.; Pacchioni, G.; Risse, T.; Freund, H. J. Interaction of gold clusters with color centers on MgO (001) films. *Angew. Chem., Int. Ed.* 2006, 45, 2630–2632.
- [36] Sun, Y. N.; Giordano, L.; Goniakowski, J.; Lewandowski, M.; Qin, Z. H.; Noguera, C.; Shaikhutdinov, S.; Pacchioni, G.; Freund, H. J. The interplay between structure and CO oxidation catalysis on metal-supported ultrathin oxide films. *Angew. Chem., Int. Ed.* 2010, 49, 4418–4421
- [37] Widmann, D.; Behm, R. J. Active oxygen on a Au/TiO₂ catalyst: Formation, stability, and CO oxidation activity. *Angew. Chem., Int. Ed.* 2011, 50, 10241–10245.
- [38] Hou, Z. Q.; Dai, L. Y.; Deng, J. G.; Zhao, G. F.; Jing, L.; Wang, Y. S.; Yu, X. H.; Gao, R. Y.; Tian, X. R.; Dai, H. X. et al. Electronically engineering water resistance in methane combustion with an atomically dispersed tungsten on PdO catalyst. *Angew. Chem., Int. Ed.* 2022, 61, e202201655.
- [39] Khoobiar, S. Particle to particle migration of hydrogen atoms on platinum-alumina catalysts from particle to neighboring particles. *J. Phys. Chem.* **1964**, *68*, 411–412.
- [40] Prins, R. Hydrogen spillover. Facts and fiction. Chem. Rev. 2012, 112, 2714–2738.
- [41] Schilling, A. C.; Groden, K.; Simonovis, J. P.; Hunt, A.; Hannagan, R. T.; Çınar, V.; McEwen, J. S.; Sykes, E. C. H.; Waluyo, I. Accelerated Cu₂O reduction by single Pt atoms at the metal-oxide interface. ACS Catal. 2020, 10, 4215–4226.
- [42] Kresse, G.; Hafner, J. Ab initio molecular dynamics for liquid metals. Phys. Rev. B 1993, 47, 558–561.
- [43] Kresse, G.; Furthmüller, J. Efficiency of ab-initio total energy calculations for metals and semiconductors using a plane-wave basis set. Comput. Mater. Sci. 1996, 6, 15–50.
- [44] Kresse, G.; Joubert, D. From ultrasoft pseudopotentials to the projector augmented-wave method. *Phys. Rev. B* 1999, 59, 1758–1775.
- [45] Perdew, J. P.; Burke, K.; Ernzerhof, M. Generalized gradient approximation made simple. *Phys. Rev. Lett.* 1996, 77, 3865–3868.
- [46] Monkhorst, H. J.; Pack, J. D. Special points for Brillouin-zone integrations. *Phys. Rev. B* 1976, 13, 5188–5192.
- [47] Henkelman, G.; Uberuaga, B. P.; Jónsson, H. A climbing image nudged elastic band method for finding saddle points and minimum energy paths. J. Chem. Phys. 2000, 113, 9901–9904.
- [48] Henkelman, G.; Jónsson, H. Improved tangent estimate in the nudged elastic band method for finding minimum energy paths and saddle points. J. Chem. Phys. 2000, 113, 9978–9985.
- [49] Cai, B.; Dianat, A., Hübner, R.; Liu, W.; Wen, D.; Benad, A.;

- Sonntag, L.; Gemming, T.; Cuniberti, G.; Eychmüller, A. Multimetallic hierarchical aerogels: Shape engineering of the building blocks for efficient electrocatalysis. *Adv. Mater.* **2017**, 29 1605254
- [50] Cai, B.; Sayevich, V.; Gaponik, N.; Eychmüller, A. Emerging hierarchical aerogels: Self-Assembly of metal and semiconductor nanocrystals. Adv. Mater. 2018, 30, 1707518.
- [51] Cai, B.; Eychmüller, A. Promoting electrocatalysis upon aerogels. Adv. Mater. 2019, 31, 1804881.
- [52] Huang, W. X.; Johnston-Peck, A. C.; Wolter, T.; Yang, W. C. D.; Xu, L.; Oh, J.; Reeves, B. A.; Zhou, C. S.; Holtz, M. E.; Herzing, A. A. et al. Steam-created grain boundaries for methane C–H activation in palladium catalysts. *Science* 2021, 373, 1518–1523.
- [53] Hickling, A.; Vrjosek, G. G. Anodic oxidation of palladium. *Trans. Faraday Soc.* **1961**, *57*, 123–129.
- [54] Garche, J.; Dyer, C. K.; Moseley, P. T.; Ogumi, Z.; Rand, D. A. J.; Scrosati, B. Encyclopedia of Electrochemical Power Sources; Elsevier: Amsterdam, 2009.
- [55] Chin, Y. H.; Buda, C.; Neurock, M.; Iglesia, E. Consequences of metal-oxide interconversion for C-H bond activation during CH₄ reactions on Pd catalysts. *J. Am. Chem. Soc.* 2013, 135, 15425–15442.
- [56] Gabasch, H.; Knop-Gericke, A.; Schlögl, R.; Borasio, M.; Weilach, C.; Rupprechter, G.; Penner, S.; Jenewein, B.; Hayek, K.; Klötzer, B. Comparison of the reactivity of different Pd-O species in CO oxidation. *Phys. Chem. Chem. Phys.* 2007, 9, 533–540.
- [57] Kim, H. J.; Lee, J. H. Highly sensitive and selective gas sensors using p-type oxide semiconductors: Overview. Sens. Actuators B: Chem. 2014, 192, 607–627.
- [58] Rogers, D. B.; Shannon, R. D.; Gillson, J. L. Crystal growth and semiconductivity of palladium oxide. *J. Solid State Chem.* 1971, 3, 314–316.
- [59] Cho, H. J.; Chen, V. T.; Qiao, S. P.; Koo, W. T.; Penner, R. M.; Kim, I. D. Pt-functionalized PdO nanowires for room temperature hydrogen gas sensors. ACS Sens. 2018, 3, 2152–2158.
- [60] Belousov, V. M.; Vasylyev, M. A.; Lyashenko, L. V.; Vilkova, N. Y.; Nieuwenhuys, B. E. The low-temperature reduction of Pd-doped transition metal oxide surfaces with hydrogen. *Chem. Eng. J.* 2003, 91, 143–150.
- [61] Gao, Z. M.; Wang, T. Q.; Li, X. F.; Li, Q.; Zhang, X. M.; Cao, T. L.; Li, Y. N.; Zhang, L. Y.; Guo, L.; Fu, Y. Pd-decorated PdO hollow shells: A H₂-sensing system in which catalyst nanoparticle and semiconductor support are interconvertible. ACS Appl. Mater. Interfaces 2020, 12, 42971–42981.
- [62] Yang, S.; Li, Q.; Li, C.; Cao, T. L.; Wang, T. Q.; Fan, F. Q.; Zhang, X. M.; Fu, Y. Enhancing the hydrogen-sensing performance of p-type PdO by modulating the conduction model. ACS Appl. Mater. Interfaces 2021, 13, 52754–52764.